

Perovskite Solar Cells with All-Inkjet-Printed Absorber and Charge Transport Layers

Fabian Schackmar,* Helge Eggers,* Markus Frericks, Bryce S. Richards, Uli Lemmer, Gerardo Hernandez-Sosa, and Ulrich W. Paetzold*

One of the key challenges of perovskite photovoltaics is the scalable fabrication of high-efficiency perovskite solar cells (PSCs). Not only the scalable deposition of high-quality perovskite thin-films itself, but also the adjacent charge extraction layers is pivotal. In this work, PSCs based on all-inkjet-printed absorber and extraction layers are presented, allowing for a scalable and material-efficient deposition. The inkjet-printed PSCs are of p–i–n-architecture with a precursor-based nickel oxide hole-transport layer, a high-quality inkjet-printed triple-cation (methylammonium, formamidinium, and cesium) perovskite absorber layer and a double layer electron-transport layer of phenyl-C61-butyric acid methyl ester and bathocuproine. The ink properties, inkjet parameters, and annealing procedure are optimized for each layer. PSCs with such inkjet-printed absorber and charge carrier extraction layers demonstrate an efficiency of >17% with low hysteresis. Although printed in ambient atmosphere, the devices show excellent short-term stability (40 h) even under elevated temperature (85 °C). These results are a promising next step on the way to fully inkjet-printed perovskite solar cells, including both electrodes as well.

1. Introduction

The power conversion efficiency (PCE) of incident solar irradiation to electrical power is the key indicator to rate photovoltaic (PV) technologies. Due to rapid increase in reported best research-cell PCEs over the past decade, the field of hybrid organic–inorganic lead halide perovskite PV has attracted enormous attention within the PV community. PCEs of up to 25.2% are certified for perovskite solar cells (PSCs) on laboratory scale, narrowing the gap toward the record for crystalline silicon solar cells of >26% although there is still a significant difference in the active area size.^[1–3] Tandem cells combining low-bandgap silicon bottom solar cells and wide-bandgap perovskite top solar cells promise PCEs exceeding the Shockley–Queisser limit of single cells^[4,5], with current record devices already achieving over 29%^[1,6–8]. However,


in order to commercialize perovskite PV as single-junction- or tandem-PV-technology, strategies to upscale PSCs while maintaining high PCEs have to be developed. There are two competing technical approaches for upscaling perovskite photovoltaics: On the one hand all-evaporated PSCs using vacuum-based deposition techniques^[9,10] and on the other hand solution-based coating and printing techniques for PSCs^[11]. Scalable solution-based techniques that have been employed in recent years are blade coating^[12,13], slot-die coating,^[14,15] and inkjet printing^[16–20]. While all of these techniques promise fast and scalable material deposition, inkjet printing stands out due to the precise control of small droplets allowing free choice of printing patterns^[21,22] and efficient material usage.^[23] Inkjet printing has already demonstrated its potential for fully-printed organic solar cells^[24,25] and organic photo detectors^[26]. Moreover, it is recently on the rise for mass fabrication of displays with organic light emitting diodes^[27–31]. PSCs with an inkjet-printed (IJP) perovskite absorber layer demonstrated steadily increasing PCEs over the past years resulting in maximum PCEs of over 21% in single scan measurements and over 18% stabilized power conversion efficiency (SPCE), as we showed in our previous publication.^[22] However, PSCs not only consist of the perovskite absorber layer, but also charge transport layers and electrodes. In contrast to many other deposition techniques for transferring the promising results on IJP perovskite layers to an industrial-scale fabrication,

F. Schackmar, H. Eggers, Prof. B. S. Richards, Prof. U. Lemmer, Dr. G. Hernandez-Sosa, Dr. U. W. Paetzold
Karlsruhe Institute of Technology (KIT)
Light Technology Institute (LTI)
Engesserstrasse 13, Karlsruhe 76131, Germany
E-mail: fabian.schackmar@kit.edu; helge.eggers@kit.edu; ulrich.paetzold@kit.edu

F. Schackmar, H. Eggers, M. Frericks, Prof. U. Lemmer, Dr. G. Hernandez-Sosa
Innovation Lab
Speyerer Strasse 4, Heidelberg 69115, Germany

F. Schackmar, H. Eggers, Prof. B. S. Richards, Prof. U. Lemmer, Dr. U. W. Paetzold
Karlsruhe Institute of Technology (KIT)
Institute of Microstructure Technology (IMT)
Hermann-von-Helmholtz-Platz 1, Eggenstein-Leopoldshafen 76344, Germany

M. Frericks
Technische Universität Darmstadt
Otto-Berndt-Straße 3, Darmstadt 64287, Germany

 The ORCID identification number(s) for the author(s) of this article can be found under <https://doi.org/10.1002/admt.202000271>.

© 2020 The Authors. Published by WILEY-VCH Verlag GmbH & Co. KGaA, Weinheim. This is an open access article under the terms of the Creative Commons Attribution License, which permits use, distribution and reproduction in any medium, provided the original work is properly cited.

DOI: 10.1002/admt.202000271

the deposition of all layers by inkjet printing allows to maintain or even extend design advantages. Although there are some reports on IJP electron transport layers (ETLs)^[32–35] and hole transport layers (HTLs)^[33,36–38], developing fully IJP PSCs remains a challenge considering the broad range of complexities that arise regarding solvent-material interactions, wetting behavior, as well as limits in annealing temperatures of each layer when processed on top of the underlying layers. While good progress on PSCs with all-IJP charge carrier extraction layers and absorber layers (in this work referred as “active layers”) is reported in the literature^[39], to the authors’ knowledge neither an average PCE > 10% nor short-term SPCEs have been shown.

In response to this challenge, this work reports on the development of PSCs with all-IJP active layers on the basis of a p–i–n-architecture. Champion devices demonstrate PCEs up to 17.2% with low hysteresis and a SPCE of 17%. The study reports on the detailed characterization of each IJP layer (HTL, absorber, double-layer ETL; the front and back-electrode are evaporated) with regard to the optical and electrical properties as well as key deposition parameters. Scalability and freedom in design of printing patterns is presented by prototype devices.

2. Inkjet-Printed Solar Cell Architecture

Reports on PSCs over the last years demonstrate a multitude of promising layer stacks arranged in two different architectures. Commonly, the community distinguishes between an n–i–p-architecture with the electron extracting n-type layers on the sun-facing transparent front-side (superstrate geometry) and a p–i–n-architecture with the hole extracting p-type layer on the transparent front-side. To date, the record PCEs of PSCs in the p–i–n-architecture lag behind those of PSCs in n–i–p-architecture^[40,41]. This usually attributed to defect-assisted recombination losses decreasing the open-circuit voltage^[42], a problem which might be solved if the architecture is investigated in more detail. Recently the p–i–n-architecture is attracting increasing attention, Ne as it exhibits low hysteresis-behavior in the *JV*-characteristics^[41] and is preferred for monolithic two-terminal perovskite/ Si tandem solar cells.^[43–45] Another reason is that the in n–i–p-architecture commonly used organic small-molecule HTL based on 2,2',7,7'-tetrakis[*N,N*-di(4-methoxyphenyl)amino]-9,9'-spirobifluorene (spiro-OMeTAD) usually contains moisture sensitive Li- or Co-containing salts. Moreover, perovskite-damaging additives (4-*tert*-butylpyridine) are used as dopants, which are considered detrimental for the stability of PSC.^[46] The choice of other HTLs in the n–i–p-architecture is not only limited by the material properties, but also by limitations in solvents and/ or annealing temperature that might damage the underlying perovskite layer. In the p–i–n-architecture, the choice of HTL materials is less constrained by choice of solvent and annealing temperature, since the HTL is processed directly on the front-electrode. Common HTLs in this architecture are poly-(3,4-ethylenedioxythiophene):polystyrene sulfonate (PEDOT:PSS)^[47,48], poly[*bis*(4-phenyl)(2,4,6-trimethylphenyl)amine] (PTAA)^[49–51] and nickel oxide (NiO_x)^[52]. In particular, solar cells with NiO_x exhibit promising performance for solution-^[53,54] as well as evaporation-based^[9,55] deposition methods when combined with an IJP perovskite

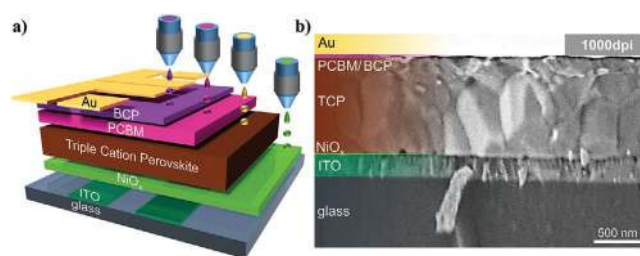


Figure 1. a) Schematic of the p–i–n-perovskite solar cell architecture with printed absorber and extraction layers: On the glass substrates (blue) with sputtered indium tin oxide (ITO, dark green) front-electrode, the HTL nickel oxide (NiO_x, light green), the triple-cation perovskite absorber layer (TCP, brown) and the double layer ETL made of PCBM and BCP (pink and purple, respectively) are deposited by inkjet printing. An evaporated Au back-electrode completes the device; b) SEM image of a cross-section through the device (TCP printed with 1000 dots per inch (dpi)).

layer^[22]. For this reason, the present work focuses on NiO_x as HTLs prepared by inkjet printing of a precursor ink. Similar to the limitations in choice for HTLs in the n–i–p-architecture, the number of materials that can be processed on the perovskite–here a triple-cation perovskite (TCP) with targeted ratio of Cs_{0.10}FA_{0.75}MA_{0.15}Pb(Br_{0.15}I_{0.85})₃–as ETL is limited. An established double-layer ETL in the p–i–n-architecture is the C₆₀-fullerene (C₆₀) combined with a very thin interfacial layer of bathocuproine (BCP) to enhance electron extraction.^[22,40,46,56,57] Although in most cases C₆₀ is thermally evaporated^[58], there are examples of solution-processed C₆₀ in the literature^[59–62], including IJP C₆₀ layers^[63]. However, due to restrictions on the inkjet-printability of C₆₀–often crystal-like solid particles instead of a closed C₆₀ thin-film are formed while drying (see more detailed discussion in the Supporting Information),–in this work [6,6]-phenyl-C₆₁-butyric acid methyl ester (PC₆₀BM, PCBM) is used. The PSCs presented in this work are finalized by an evaporated gold (Au) back-electrode (**Figure 1a**). A scanning electron microscopy (SEM) image of a cross-section through the device architecture glass/indium tin oxide (ITO)/ NiO_x/TCP/PCBM/BCP/Au is shown in **Figure 1b**. The band-gaps and energy levels of the single layers used in the stack are expected to allow for an efficient charge transport throughout the device, not taking any band bending effects at the interfaces into account (**Figure S1**, Supporting Information). In this work, with exception of the Au and ITO electrodes, all layers (here referred to as “active layers”) are deposited by inkjet printing.

3. Inkjet Printing of Perovskite Solar Cells

3.1. Working Principle of Inkjet Printing

Drop-on-demand inkjet printing requires mastering three key challenges: 1) Stable jetting of the ink: in piezoelectric-driven print heads, a time dependent voltage pulse (a so-called waveform) is applied to a piezoelectric element inside the ink-filled nozzle that creates a mechanical pulse due to its deformation. In order to eject well-shaped droplets with this pulse, the viscosity and surface tension (SFT) of the solution in the nozzle (so-called ink) needs to be in a distinct range and ratio.^[23,64] Printing of nanoparticle (np) dispersions/sol-gels requires a

small enough diameter of the used particles to avoid clogging of the nozzle. The 2) drop-substrate interaction starts, when the ejected droplets are deposited onto the substrate. The shape of the droplet deposited on top of the substrate is determined by its adhesion to the substrate (dependent on the surface free energy (SFE) of the substrate) and cohesion of the droplet (dependent on the SFT of the ink), which is quantified by the contact angle (θ_{contact}) between liquid and solid. The SFT of the ink and the SFE of the substrate need to be engineered to avoid spreading (so-called over-wetting, $\theta_{\text{contact}} = 0^\circ$) on the one side and receding of the droplet (so-called de-wetting) on the other. The as-printed droplets form the wet-film on the substrate. 3) Drying and annealing of the wet film determines the shape and morphology of the deposited thin-film. Two aspects need to be balanced: first, the volume flow toward the edge of the wet-film leading to an edge-enriched particle agglomeration, the so-called coffee ring. The second aspect to be considered is an undesired contraction toward the center of the wet-film. In the case of poly-crystalline materials like perovskite thin-films, drying and annealing are even more important, since the optoelectronic properties depend on nucleation and crystal growth.^[11,65]

The above detailed steps are interrelated, making inkjet printing of a multilayered PSC architecture a complex process that needs iterative optimization. In the following, we will report on the stepwise optimization of each of these challenges for the four individual thin-films in our p-i-n-architecture.

3.2. Inkjet-Printed Nickel Oxide Hole-Transport-Layer

Several solution-based deposition methods for inkjet printing of NiO_x layers have been reported for non-PV applications as p-type semiconductor^[66–69] and as HTL in thin-film PV^[36,37,70] either on the basis of NiO_x nanoparticles dispersions^[37,66,67] or on basis of precursor solutions^[36,68–70]. In this work, we use the precursor material nickel(II) acetate dihydrate (NiAc), which is deposited as a sol-gel and subsequently decomposed during an annealing step in ambient atmosphere containing oxygen to form non-stoichiometric NiO_x. For the decomposing process of NiAc, temperatures below 300 °C have been reported.^[69,71,72] The process is therefore compatible with the underlying ITO substrate, taking into account that the degradation of ITO starts at temperatures around ≈250–325 °C.^[73,74] Most alternative IJP NiO_x precursor material systems require substantially high annealing temperatures (>400 °C), which are not compatible with the ITO-coated substrate.^[68,70] Although alternative transparent conductive oxides like fluorine-doped tin oxide (FTO) withstand these temperatures, they exhibit a lower conductivity at same mean transmittance values.^[75] An established low-temperature alternative are IJP NiO_x nanoparticle (≈7–200 nm diameter) thin-films^[37,66,67,76], which are challenging to process as nanoparticles are prone to cause agglomerations and clogging of the inkjet nozzles.^[77] In this work, we developed a 1-butanol:ethanol-based NiAc ink with addition of the ligand monoethanolamine (see the Experimental Section). This ink has a sufficient high boiling point to allow printing at 5 kHz with drop velocities $v_{\text{droplet}} \approx 3 \text{ mm s}^{-1}$ (see Figure S2a, Supporting Information). The wetting behavior of this ink on the ITO substrate can be estimated by calculating wetting envelopes according to Owens, Wendt, Rabel, and Kaelble

(OWRK) method^[78–80], which display a constant θ_{contact} (in this case $\theta_{\text{contact}} = 0^\circ$) for the SFE of the substrate, split into its polar and dispersive part. On non-treated substrates, the as-printed wet-film does not spread homogeneously and exhibits holes due to dirt or local wetting differences. As a result, a multi-cycle cleaning process has been introduced (see the Experimental Section). The wetting envelopes of an untreated and cleaned ITO substrate show the overall increase in the SFE via this surface treatment (Figure 2a). Although the SFT_{NiAc Ink} is low (≈21 mN m⁻¹), the wetting on the treated ITO substrate is optimal, leading to ≈100 μm drop diameters and convenient sharp edges at a printing resolution of 700 dpi (dots per inch). Using an ink based on a mixture of butanol and ethanol allows for the deposition of printing-stripe-free NiO_x thin films. This effect is similar to reported addition of glycerol to suppress the printing stripes of a 2-methoxyethanol NiAc ink.^[36,69]

Annealing of the precursor thin film is important for the transformation of the wet-film into a conductive transparent NiO_x thin-film. In the literature, a large variety of annealing temperatures have been reported ranging from 230 to 400 °C^[36,69] for sufficient and optimal decomposition. Singh et al. performed a thermogravimetric analysis of NiAc thin-films and detected two loss regimes, with the first one appearing around 100 °C attributed to evaporation of embedded water molecules and the second one around 350 °C attributed to loss of water through decomposition to NiO_x.^[36] Therefore, we analyzed samples annealed at 190 °C (directly after the first loss regime), 280 °C (above the temperature for complete conversion to NiO_x according to ref. [71]) and 325 °C (in the second loss regime) as annealing temperatures while maintaining a constant annealing time of 45 min. Annealing at temperatures of 400 °C (after the second loss regime) leads to a reduction in the transmittance of the ITO front-electrode and an increase in series resistance R_{Series} of the PSCs, indicating the decomposition of ITO (Figure S3, Supporting Information).

The morphology of the IJP NiAc thin-films annealed at the three different temperatures was investigated using atomic force microscopy (AFM). No structural differences are apparent, with a similar root-mean-square (RMS) roughness of $R_q \approx 3 \pm 0.5 \text{ nm}$ for all samples (Figure 2b). The RMS roughness of the NiO_x layers is lower than the one of plain ITO ($R_q \approx 3.8 \pm 0.7 \text{ nm}$), indicating a smoothing effect of the NiAc ink. The transmittance of the bottom charge transport layer in PSCs is an important characteristic, since it determines the amount of parasitic absorption losses that limit the harvestable incident radiation in the PSC. Figure 2c shows the overall high transmittance for all annealing temperatures of the glass/ITO/IJP NiAc samples. With increasing temperatures, the transmittance decreases in the wavelength range from 350 to 500 nm and >700 nm. The sample annealed at 190 °C shows a similar shape to pure glass/ITO, especially in the near bandgap area. In agreement with our findings, Hu et al. reported a shifted bandgap with increasing annealing temperature (3.82 eV at 180 °C to 3.67 eV at 330 °C)^[69]. Compared to electron beam (e-beam)-evaporated NiO_x thin-films developed in the work of Abzieher et al.^[55] and used for IJP high-efficiency PSCs^[22], the mean solar-weighted transmittance between 325 and 800 nm of the IJP thin-films is 2.3% lower (≈81.2% T_{sw} vs ≈83.5% T_{sw} , for calculation see the Experimental Section).

To determine the conductivity, we performed resistivity measurements on the IJP NiAc thin-films annealed at three

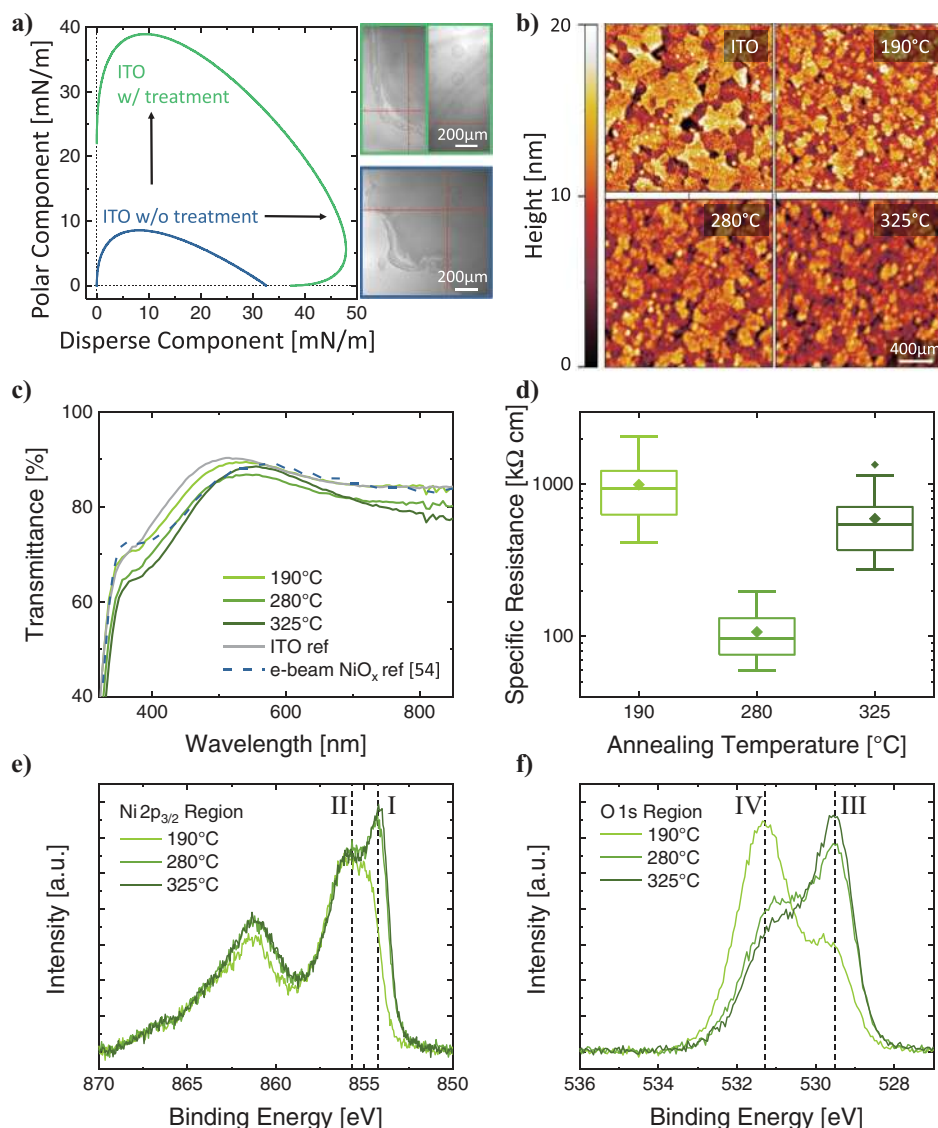


Figure 2. Inkjet-printed NiAc for NiO_x hole transport layers: a) Wetting envelopes (for a contact angle $\theta_{\text{contact}} = 0^\circ$) of an uncleaned and a glass/ITO substrate, treated with a multistep cleaning cycle increasing polar and disperse part of the surface free energy (SFE) and the corresponding printer camera top-view images of a printed square (700 dpi) and single dots; b) Atomic force microscopy (AFM) images, c) transmittance, d) specific resistance, e) photoelectron spectrum of the Ni 2p_{3/2} and f) O 1s region of IJP NiO_x thin-films on glass/ITO annealed at 3 different temperatures.

temperatures and calculated the specific resistance (Figure 2d). Annealing at 280 °C leads to the lowest resistance, while samples annealed at 190 and 325 °C exhibit higher resistance. A similar trend was previously observed for charge carrier mobilities of IJP NiAc thin-films on Al₂O₃. For thin-films annealed at 180 °C, low mobilities were reported, whereas a maximum mobility was reached for 280 °C annealed samples and for higher annealing temperatures, the mobilities decreased again.^[69]

For a better understanding of the conversion of the NiAc thin-films annealed at the three different temperatures, high resolution X-ray photoelectron spectra of the Ni 2p_{3/2} and O 1s region (Figure 2e,f) were analyzed. Besides the satellite structure above 860 eV, the spectra of the Ni 2p_{3/2} region, feature two distinct maxima around ≈854.3 eV (I) and ≈855.7 eV (II). Considering the spectra for NiO and Ni(OH)₂ reported by Grosvenor

et al., the first maximum (I) is a clear indication for NiO while the second maximum (II) cannot be solely assigned to a single phase, but might contain contributions of both.^[81] Consequently, annealing the NiAc thin-films at a temperature of 190 °C results only in a negligible conversion to NiO, while the NiAc thin-films annealed at 280 and 325 °C display unambiguously the presence of NiO. The analyses of the O 1s emission spectra support these findings: The maximum at ≈529.5 eV (III) is attributed to O²⁻ present in NiO and the maximum at ≈531.3 eV (IV) is associated to OH⁻ present in Ni(OH)₂.^[72,82–84] While the NiAc thin-film annealed at 190 °C exhibits a dominant OH⁻ peak, the NiAc thin-films annealed at 280 °C show the conversion to NiO that seem to proceed further at the higher annealing temperatures of 325 °C. The variation in the intensities is related to an existing difference in the defect chemistry of the formed NiO

layer for higher temperatures. Apart from the photoemission spectra shown in Figure 2, measurements of the C 1s region indicate remaining C–O and C–C species^[85] for the NiAc thin-films annealed at 190 °C. Moreover, UV-photoelectron spectra of the valence band exhibit a reduction of the energy difference of the Fermi level to the valence band maximum of about 300 meV compared to the higher annealing temperatures (see Figure S4, Supporting Information). Taking all spectral information into account, a more complete conversion of NiAc to NiO at the higher annealing temperatures is evident.

Device performance data supports these findings, where devices annealed at 190 °C showed an S-shaped characteristic, which we relate to the insufficient conversion to NiO_x (NiO_x, since no conclusion can be drawn regarding the stoichiometric Ni:O ratio) as shown above. A discussion on the origin of the S-shape can also be found in literature.^[86,87] At ≈325 °C annealed PSCs exhibited a higher *R*_{series} originating from ITO degradation (see Figure S5, Supporting Information). For these reasons, we chose 280 °C as annealing temperature in the here presented fabrication process. Comparison with PSCs utilizing an e-beam-evaporated NiO_x thin-films display a decreased open-circuit voltage *V*_{oc} for devices with IJP NiO_x thin-films (Figure S6, Supporting Information), which could be attributed to the incomplete conversion of the precursor.

3.3. Inkjet-Printed Triple-Cation Perovskite Absorber Layer

Subsequent to the HTL, the perovskite absorber layer is printed. The recipe used in this work for printing the

Cs_{0.1}FA_{0.75}MA_{0.15}(I_{0.75}Br_{0.15})₃ triple-cation perovskite (TCP) absorber layers was described in detail in ref. [22]. As ink, a formamidinium (FA), methylammonium (MA), and cesium (Cs) based 0.75 M precursor solution in the polar-aprotic solvent system *N,N*-dimethylformamide (DMF), dimethyl sulfoxide (DMSO), and γ -butyrolactone (GBL) is IJP in ambient environment (≈20 °C, ≈45% relative humidity) (for details, see the Experimental Section, for jetting analysis see Figure S2b, Supporting Information). The SFE of the pristine IJP NiO_x layer is too high for our TCP ink system, leading to uncontrolled spreading of the ink and drop diameters of ≈200 μ m. Therefore, we reduced the SFE by an isopropanol (IPA) washing treatment, which is evident by a shift of the corresponding wetting envelope (Figure 3a) and more descriptively by the underlying change of contact angle (compare Figure S7, Supporting Information). This enables well-shaped, hole-free IJP wet-films and drop diameters around ≈100 μ m (Figure 3a). The layer is printed in ambient air at room temperature in a single-pass printing process. Subsequent to the printing, the wet-film is transferred to a vacuum chamber and vacuum-annealed for a few minutes (≈2–10 min) to extract the solvents. Although no elevated temperature is applied here, this process will be referred to as vacuum annealing in this manuscript since it induces and determines nucleation and crystallization of the perovskite. Subsequently a second thermal annealing step outside of the vacuum is used. By combination of these two annealing steps, ≈1.0 μ m thick, multicrystalline perovskite thin-film is formed (Figure 1b). As analyzed in a previous study, the printed resolution (corresponding to the wet-film thickness) determines not only the perovskite thin-film thickness, but also

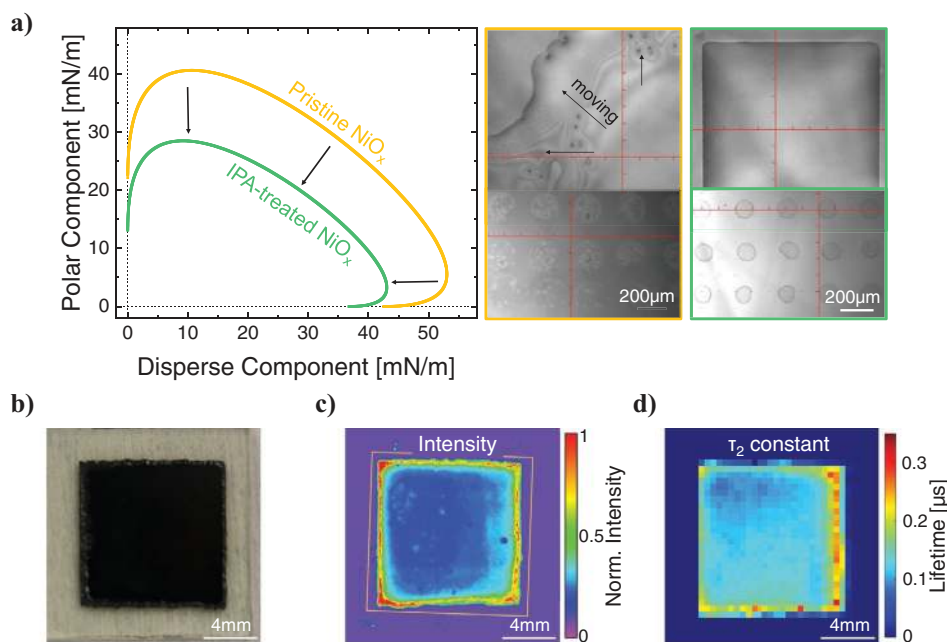


Figure 3. Inkjet-printed triple-cation perovskite (TCP) absorber layer: a) Left: Wetting envelope (for $\theta_{\text{contact}} = 0^\circ$) of an untreated and an IPA-washed glass/ITO/IJP NiO_x surface, which reduces the SFE. Right: Corresponding printer camera top-view images of a printed square (1000 dpi) and single dots; b) Photography of an IJP TCP layer on top of the IJP NiO_x surface; c) steady state photoluminescence (PL) image (normalized to the maximum grey value in the yellow indicated square) and d) spatial distribution of the lifetime constant τ_2 retrieved by a biexponential fit of multiple time-resolved PL measurements (30 × 30 pixel) of an 11 × 11 mm² IJP TCP thin-film on glass/ITO/NiO_x.

influences absorber crystallization and surface stoichiometry.^[22] Throughout the remainder of this work, we use 1000 dpi, as this results in the best compromise between high fill factors (800 dpi) and high current density (1100 dpi) of the PSCs.

At first glance, IJP TCP square areas of $11 \times 11 \text{ mm}^2$ appear homogeneous (Figure 3b). A more detailed investigation is done using photoluminescence (PL) imaging. To quantify the homogeneity, a photoluminescence (PL) pseudo-color image of an unstructured glass/ITO/ NiO_x substrate is shown in Figure 3c. The thicker coffee ring at the edges ($\approx 0.5\text{--}1 \text{ mm}$ wide, compare Figure S8, Supporting Information) leads to brighter emission, surrounding a more smooth and homogeneous area in the center of the square, where the active areas of the later solar cells are located. Small spots of relatively higher or lower signal intensity indicate small impurities in the layer that are not visible by conventional surface characterization via SEM or AFM (compare surface morphology in Figure S9, Supporting Information). Additionally, the absorber is analyzed using sequential time-resolved PL mapping (Figure 3d). The transient PL decay at each spot is quantified by extracting the lifetime constant τ_2 of a biexponential fit^[88–91] (see the Experimental Section for details and Figure S10 (Supporting Information) with PL decay plots for exemplary coordinates). The increased lifetime constants at the edges result from the coffee ring-related higher film thicknesses in agreement with the findings reported in our previous work.^[22] The inner square shows a sufficient homogeneous spatial distribution ($\tau_{2,\text{mean}} \approx 0.12 \mu\text{s} \pm 0.01 \mu\text{s}$, histogram in Figure S11, Supporting Information).

3.4. Inkjet-Printed PCBM/BCP Electron-Transport-Layer

At last, a double layer ETL is IJP. The first layer is the fullerene derivative PCBM, which is a common solution-processed ETL in PSCs^[47,58,92–96], and the second layer is BCP. We use PCBM instead of the more common C_{60} as ETL, as PSCs with IJP C_{60} thin-films demonstrated poor performance (see more detailed discussion in the Supporting Information and Figure S12, Supporting Information). The PCBM ink solvent system employed is composed of 1,2-dichlorobenzene:mesitylene (oDCB:MT 3:1 volume ratio), in order to reduce the high SFT of oDCB.^[97–99] Similar inks compositions have been established for polymer:fullerene blends for IJP absorber layers of organic solar cells.^[97–100] The aromatic solvents allow processing on the underlying multicrystalline perovskite layer. An ink with PCBM concentration of 10 mg mL^{-1} allows stable drop generation (see Figure S2c, Supporting Information).

Since most polar reference solvents for θ_{contact} measurements like DMSO, ethylene glycol and water destroy the perovskite thin-film, the SFE of the underlying IJP TCP layer cannot be determined in the established approach used before (Figures 2a and 3a). Nevertheless, taking into account the low contact angle of the nonpolar, high-SFT solvent diiodo methane (DIM) $\theta_{\text{contact, DIM}} \approx 26^\circ$ (Figure 4a), the SFE of the perovskite thin film must be comparably high. Consequently, the PCBM ink shows over-wetting behavior on the IJP TCP surface. In contrast, preferable wetting behavior on IJP NiO_x surfaces, allows well-shaped printed features (Figure 4b). We exploit this distinctly different wetting behavior of the two surfaces with

different SFE to achieve hole free PCBM wet-films on the TCP surface with well-defined edges of the wet-film on the NiO_x surface. The wet-film is dried in a vacuum chamber, resulting in good uniformity as reported similarly in literature^[97–99].

As for C_{60} , PCBM ETLs are usually used in combination with thermally evaporated interfacial layers like LiF ^[101] or BCP ^[46]. Here, we adapt a solution-based approach^[102] using 0.5 mg mL^{-1} BCP in EtOH as ink. According to basic solubility calculations and experimental evidence^[103] the underlying PCBM is assumed to be insoluble to the EtOH. This so-called orthogonality of layers and solvents is of utter importance for every of the successively printed layer in general and was checked for every printing step. The boiling point and SFT of EtOH are at the lower limit of the theoretical inkjet criterion for stable jetting of the ink, which is nonetheless possible at 2000 Hz without any additive (see Figure S2d, Supporting Information). Figure 4c shows IJP BCP single dots on top of IJP $\text{NiO}_x/\text{TCP}/\text{PCBM}$ with $\approx 100 \mu\text{m}$ in diameter and three squares printed in different resolutions. While well-defined squares are printed for resolutions of 800 dpi, a significant bulging is apparent for 1000 dpi and 1200 dpi.

To achieve high performance PSCs, the IJP PCBM/BCP double layer needs to be optimized in thickness: One the one hand, the PCBM wet-film has to be sufficiently thick such that the resulting PCBM thin film covers well the underlying perovskite layer, while on the other hand the series resistance R_{series} increases with thickness. To find the optimal trade-off, we prepared IJP $\text{NiO}_x/\text{TCP}/\text{PCBM}/\text{BCP}$ -PSCs with PCBM layers of different resolutions and thus different thicknesses. Figure 4d shows exemplary *JV*-characteristics of these devices. In the case of 600 dpi, the open-circuit voltage V_{oc} is reduced by $\approx 0.1 \text{ V}$ as compared to 800 dpi, indicating the PCBM layer is too thin or has too many holes, while for 1000 dpi and 1200 dpi the R_{series} increases and the FF drops (see Figure S13 and Table S14, Supporting Information). Comparison of devices with spin-coated PCBM layers display a significantly lower shunt resistance R_{shunt} for PSCs with IJP PCBM (compare Figure S15 and Table S16, Supporting Information) supporting the hypothesis that holes are still present in the IJP thin film. While the corresponding thicknesses on the TCP layer are difficult to determine, thickness estimations of IJP PCBM on glass suggest layer thicknesses of 11 nm (600 dpi), 18 nm (800 dpi), and 30 nm (1000 dpi). For optimization of the BCP layers IJP on top of the layer stack, there is no significant difference in maximum performance for the 800 dpi, 1000 dpi, and 1200 dpi resolutions apparent. All devices with printed BCP, independent of the resolution, demonstrate higher FFs as a result of better charge extraction compared to devices without BCP (Figure S17, Supporting Information). Here, 1000 dpi printed BCP layers lead to higher average PCE (Figure 4e). As such, we chose 1000 dpi compromising between a well-defined printing area and the probability of pinholes.

4. Performance of Inkjet-Printed Solar Cells

Having discussed the sequential inkjet-printing of all active layers, we evaluated the performance of IJP PSCs. Figure 5a shows the *JV*-characteristics of a 10.5 mm^2 small-active-area

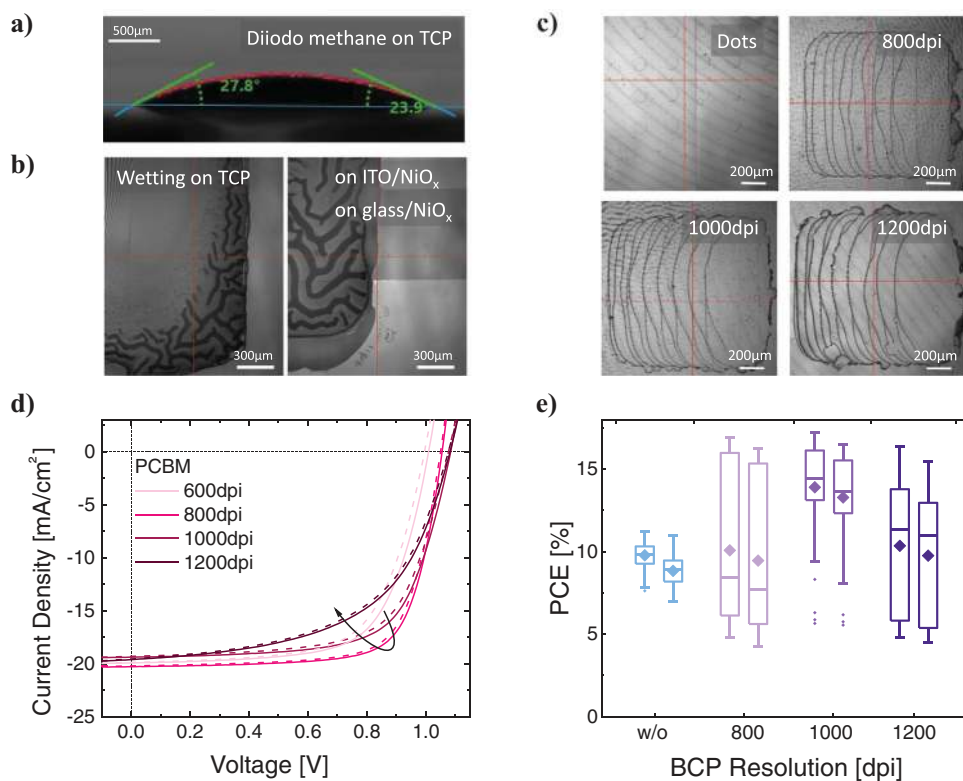


Figure 4. Inkjet-printed PCBM electron transport layer and BCP interfacial layer: a) low contact angle (θ_{contact}) of $\approx 26^\circ$ for diiodo methane, indicating a high SFE of the TCP surface; b) (left) wetting of the PCBM ink on the IJP TCP layer ($\theta_{\text{contact, PCBM ink}} \approx 0^\circ$, spreading of the ink that stops at the perovskite border) and (right) on glass/(ITO)/NiO_x ($\theta_{\text{contact, PCBM ink}} > 5^\circ$, receding contact line); c) IJP BCP on glass/ITO/NiO_x/TCP/PCBM, IJP single pixel dots with a diameter of $\approx 100 \mu\text{m}$ and in different resolutions printed squares showing a coffee ring drying behavior; d) Current density–voltage (*JV*) characteristics (exemplary curves; FW is dashed, BW solid) and e) PCE boxplot distribution of the of IJP NiO_x/TCP/PCBM/BCP PSCs showing the influence of PCBM respective BCP printed in different resolutions (wet-film thicknesses; left box BW, right box FW for each resolution).

champion device, exhibiting a PCE of 17.2% in backward (BW) scan direction (the PCE in forward (FW) scan direction is 16.5%) with a hysteresis index factor HIF ≈ 0.96 (described in the Experimental Section). Moreover, the SPCE was determined by MPP-tracking over 10 min at 25 °C in nitrogen atmosphere, reaching values up to 17%. These remarkable device characteristics demonstrate the prospects of IJP PSC, for example in comparison to PCEs reported in literature for i) PSCs with IJP active layers^[39] (n–i–p-compact-architecture, 10.7% PCE, 0.6 HIF, no SPCE shown) and ii) partially IJP active layers (mesoporous n–i–p-architecture, spin-coated HTL, 14.1% PCE, 0.81 HIF, no SPCE shown). The considerable FFs around 70% highlight the good quality of the IJP PSCs. However, compared to IJP perovskite absorber layers in PSCs with charge transport layers prepared by evaporation or by non-scalable solution-based techniques,^[18,22,55] there is significant room for improvement in FF up to $\approx 80\%$ which shall be addressed in future work. In comparison with PSCs with all-printed active layers fabricated by other scalable printing techniques like blade coating and slot-die coating both the PCE and SPCE presented in this work are one of the highest achieved so far (compare Figure S18, Supporting Information).

To investigate the power output stability of the presented IJP architecture for a prolonged time-period (>40 h), we tracked the MPP of a non-encapsulated PSC at constant temperature

(85 °C) in nitrogen atmosphere (Figure 5c). The SPCE shows constant power output for >40 h, demonstrating that the developed architecture is capable to withstand elevated temperatures. Reports on MPP tracking measurements of IJP perovskite absorber layers over time-scales >1 h are rare, with Liang et al. reporting around 70% PCE preservation after 40 h constant illumination in a photo stability test^[17] and Eggers et al. reporting no loss after 70 h MPP tracking at 25 °C^[22].

As the next step toward up-scaling, 100 mm² active-area PSCs were examined, including the entire homogeneous area of the IJP perovskite absorber (121 mm²) without the coffee ring-shaped edges. The *JV*-characteristics of a 100 mm² active-area IJP PSC and two small-area references of the same batch are shown in Figure 6a. The PCE of 12.3% achieved with the 100 mm² area PSC is within the same range of the mean value of the 10.5 mm² area reference devices prepared in the same batch ($\approx 13\%$ PCE), but there is a gap to the best-performing champion devices present. For 100 mm²-PSCs with IJP perovskite absorber layers, the preserved performance ratio $\text{PCE}(<11 \text{ mm}^2)/\text{PCE}(100 \text{ mm}^2)$ of $\approx 94\%$ is comparable ($\approx 90\text{--}97\%$), although the reported 100 mm²-PCEs are higher ($\approx 15.3\text{--}17.7\%$).^[17,104] The SPCE measurements of the same devices show a similar trend, providing a stable power output (Figure 6b). The losses in performance assumably origin in 1) the not optimized electrode properties and layout leading mainly to high series resistances and 2) small impurities in the printed

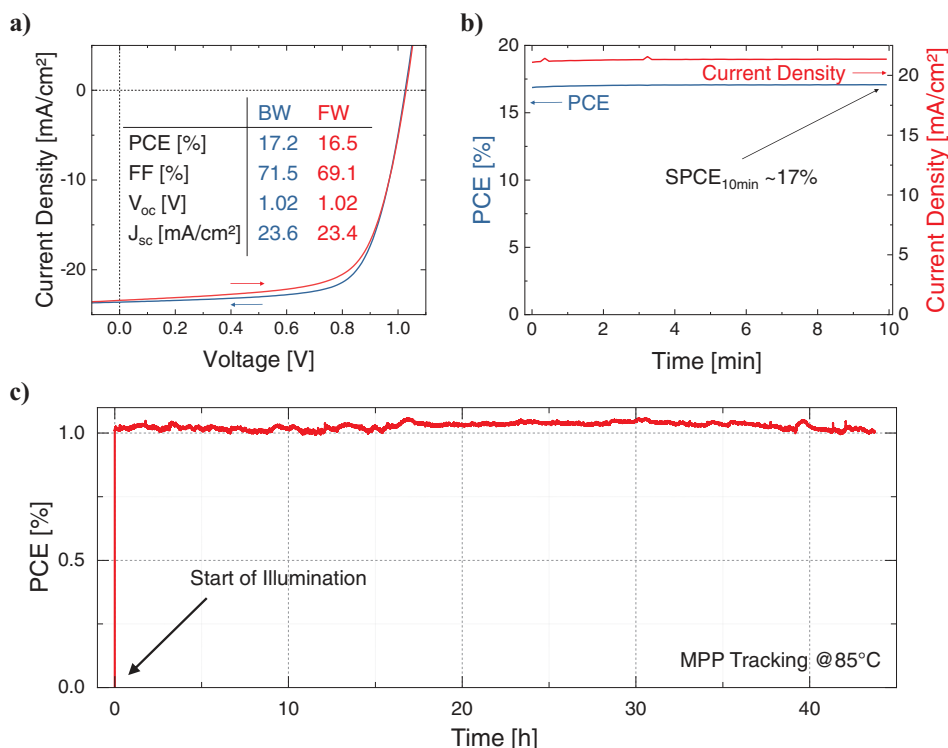


Figure 5. PV performance of IJP PSCs: a) *JV*-characteristic of the champion PSC for backward (BW) and forward (FW) scan direction demonstrating ≈17% PCE; b) maximum power point (MPP) tracking at 25 °C with a stabilized PCE (SPCE) of ≈17%; c) MPP tracking for >40 h at 85 °C normalized to the first data point after opening the light shutter, showing the behavior of the PSC directly after exposure to illumination.

film (compare Section 3.3), which might lead to pin holes and consequently lower shunt resistances and lower V_{OC} . While the first challenge can be overcome by adjustment of the device layout, for the second one some further improvements of the cleaning procedure or the printing process have to be provided in the future.

5. Conclusion

In this work, an inkjet printing process for PSC in p–i–n-architecture with all-IJP absorber and charge transport layers was introduced. We demonstrated PCEs above 17% in both

current–voltage characteristic and stabilized power output measurements (5 min, MPP tracking). Furthermore, the IJP PSC architecture exhibits a stable short-time-operated (>40 h) PCE at 85 °C with no loss in PCE. The key steps for the preparation of every printed layer from the ink preparation over the substrate preparation for optimum wetting to the drying and annealing were reported. As hole transport layer, the ITO-compatible low-temperature (<300 °C) NiO_x-precursor based on nickel acetate was inkjet-printed and optimized. For the IJP triple-cation perovskite absorber layer ((Cs:FA:MA)Pb(I:Br)₃), micrometer-thick (≈1 μm) columnar crystal structures were deposited. The homogeneity of the (11 × 11 mm²) IJP perovskite layer was

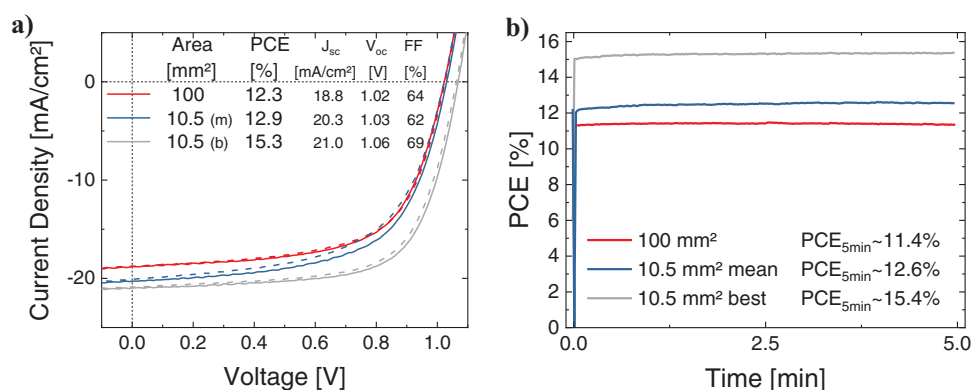


Figure 6. a) *JV*-characteristic (BW solid, FW dashed) and b) MPP tracking measurement of a 100 mm² PSC and two 10.5 mm² references (mean and best) of the same batch; the IJP areas are the same, but the size of the evaporated Au back-electrode is different.

examined by high-resolution PL images and a spatial resolved PL decay time map, indicating a homogeneous layer. The stack was finalized by an IJP double layer of PCBM as electron transport layer and BCP as interfacial layer for improved charge carrier extraction. To prove the up-scalability, a 100 mm² active area device was shown preserving ≈94% of the mean PCE of 10.5 mm² area devices. Altogether, this work demonstrates that PSCs with multiple IJP active layers can achieve remarkable performance although entirely printed in ambient atmosphere using a material-efficient printing process, suitable for nearly arbitrary patterned upscaling.

6. Experimental Section

Ink Fabrication: The 4 inks for inkjet printing are prepared as follows: 1) nickel(II) acetate tetrahydrate (99.995% trace metals basis, Sigma-Aldrich) was dissolved in anhydrous ethanol (99.8%, Bernd Kraft) to an 0.05 M solution, monoethanolamine (<98%, Sigma-Aldrich) was added 1:1 molar as a ligand^[71] and the green solution was left for 1 h on a hotplate at 60 °C. Before filling the cartridge, the ink was mixed by adding 3:1 (volume) 1-butanol (98%, Sigma-Aldrich). 2) For the perovskite ink, CH(NH₂)₂I (FAI, 0.6 M, GreatCell Solar), PbI₂ (0.66 M, Alfa Aesar, ultra dry), CH₃NH₃Br (MABr, 0.12 M, GreatCell Solar), and PbBr₂ (0.12 M, TCI Chemicals) are dissolved in a mixture of DMF (anhydrous, Sigma-Aldrich), DMSO (anhydrous, Sigma-Aldrich), and GBL (Sigma-Aldrich) in a ratio 28:26:46 (volume percentage). Additionally, CsI (1.5 M, Alfa Aesar) is dissolved in DMSO and then added to the first solution to get a 0.75 M TCP solution with the targeted composition Cs_{0.10}FA_{0.75}MA_{0.15}Pb(Br_{0.15}I_{0.85})₃^[22,105]. Before printing, the ink was filtered with a 0.45 μm pore size polytetrafluoroethylene (PTFE) filter. 3) For the PCBM ink, PC₆₀BM (purity >99.5%, Solenne BV) was dissolved to 10 mg mL⁻¹ in 1,2-dichlorobenzene (Sigma-Aldrich) and mesitylene (Sigma-Aldrich) 3:1 (volume). 4) For the BCP ink, BCP (Luminescence Technology) was dissolved in ethanol to 0.5 mg mL⁻¹.

Sample Fabrication: The following route was used for preparation of the samples: Pre-patterned ITO on glass substrates (Luminescence Technology) were cleaned consecutively in Hellmanex, deionized water, acetone, and isopropanol (IPA) in an ultrasonic bath for 5 min each, followed by an oxygen plasma-cleaning step for 5 min and again 5 min acetone and IPA in an ultrasonic bath. For inkjet printing, a Meyer Burger Pixdro LP50 with a print head module for 10 pL Fujifilm cartridges (Dimatix DMC-16610) was used in ambient conditions (≈20 °C, ≈45% relative humidity). After the substrate cleaning, the NiAc HTL is deposited (700 dpi printing resolution, 2 kHz jetting frequency) and then put on a thermocouple-controlled hotplate in air at 280 °C for 45 min. After cooling down, the samples are washed in IPA.

Subsequently, the triple-cation mixed halide perovskite (TCP) absorber layers were deposited (1000 dpi, 2–5 kHz) in a single-pass printing process as described in ref. [22]. The total area of the inkjet-printed TCP is 11 × 11 mm² per sample. Within the time frame of ≈30 s the as-printed samples were transferred to a nearby vacuum chamber (Pfeiffer Vacuum Technology AG) which is then evacuated down to ≈5 × 10⁻² mbar at room temperature. After the perovskite is formed, the chamber is slowly vented and the samples put on a hotplate at 100 °C for thermal annealing.

Then, the PCBM fullerene ETL layer is printed on top of the perovskite (800 dpi, 2 kHz), followed again by a short vacuum-assisted drying (≈1–2 min). Finally, the BCP interfacial layer is printed on top (800–1000 dpi, 2 kHz), followed by the thermal evaporation of a 75 nm thick gold back-contact using a shadow mask, which defines the active area to 10.5 mm² per solar cell with 4 cells per sample or to 100 mm² with 1 cell per sample.

Characterization—Scanning Electron Microscopy (SEM): SEM images were taken in high vacuum at 1 kV Voltage at a Zeiss Auriga system. Cross-sections of samples were prepared by cutting the rear-side of the sample and breaking the glass. Since SEM images were not corrected

for small tilts due to sample preparation, they should not be used for reliable determination of absolute thicknesses.

Characterization—Atomic Force Microscopy (AFM): The surface profiles were measured using a NanoWizard II (JPK Instruments).

Characterization—UV–Vis–NIR–Transmittance Measurements: Transmittance was measured with a spectrophotometer (Perkin Elmer Lambda 1050) with an integrating sphere. The solar-weighted transmittance is calculated using $T_{sw} = \frac{\int T \cdot \lambda \cdot E_{AM1.5G} d\lambda}{\int \lambda \cdot E_{AM1.5G} d\lambda}$ in the wavelength interval between 325 and 800 nm with 5 nm resolution, similar to ref. [106].

Characterization—Solar Cell Characteristics: For the measurement of the solar cell characteristics, i) class AAA xenon-lamp-based solar simulator (Newport Oriol Sol3A) or ii) class AAA 21-channel LED solar simulator (Wavelabs Solar Metrology Systems Sinus-70), both with an AM1.5G spectrum (100 mW cm⁻²) and inside a nitrogen-filled glovebox, were calibrated with a KG5 short pass-filtered silicon reference solar cell (data of Figures 4d, 5c, and 6 acquired with (i) and Figures 4e and 5a,b with (ii)). For JV-scans, the cells were measured in both backward and forward direction with a constant scan rate of circa 0.6 V s⁻¹ (Keithley 2400 source measurement unit) while controlling the temperature of the solar cell (JV-scans at 25 °C) using a microcontroller-adjusted Peltier-element. The maximum power point (MPP) was tracked by using a perturb-and-observe algorithm (at 25 °C or 85 °C, not the same cell is used). Hysteresis index factor HIF was calculated as fraction of PCE measured in backward- and forward-direction: $HIF = PCE_{FW}/PCE_{BW}$.

Characterization—Resistance: The resistance was measured with a source measurement unit (Keithley 2400) using the solar cell ITO/HTL/Au layout. The specific resistance is calculated taking into account the electrode area (10.5 mm²), the HTL thickness (15 ± 5 nm) and ITO/Au resistance.

Characterization—Time-Resolved Photoluminescence: A self-built PL setup with a pulsed laser (532 nm, 1 kHz repetition rate, 800 ps pulse width, ≈2 nJ pulse energy, an Acton spectrometer and a CCD camera (PIMAX512), captured normal to the surface of the layer) with a gated mode and a 2D-stage was used. The samples are measured in ambient atmosphere at room temperature, sequentially point by point. A biexponential fit $I = a_1 \exp(-t/\tau_1) + a_2 \exp(-t/\tau_2)$ was used to determine a lifetime constant τ_2 describing the radiative recombination in the bulk and the time constant τ_1 (<0.05 μs) describing nonradiative recombination such as band-to band recombination and quenching of PL by extraction of charge-carriers.

Characterization—PL Imaging: For PL imaging, a self-built setup combining a 2.1 megapixel monochrome sCMOS camera (Thorlabs CS2100M-USB Quantalux), a camera lens (Thorlabs MVL12M23) and a LED-ring (CCS HPR2-100BL) emitting blue light (emission peak at 470 nm) was used. The image was acquired through a 760 nm longpass filter.

Characterization—Photoelectron Spectroscopy: To study the conversion of NiAc, thin-film samples were prepared as above and annealed at 190, 280, and 325 °C. After annealing, each sample was transferred to a PHI 5000 VersaProbe operating at a base pressure of 10⁻⁹ mbar. Core level spectra were taken with a monochromatic Al Kα (1486.6 eV) X-ray source, while He-I radiation (21.22 eV) from a He discharge lamp was used for the ultraviolet-photoelectron spectroscopy. The secondary electron cut-off was measured with an applied bias voltage of -5 V. All spectra are calibrated to the Fermi level edge of a silver standard. A Shirley type background was subtracted from the core level spectra according to literature^[107–109].

Characterization—Surface Profiles and Thickness: The thickness for most thin-films was measured using a Bruker Dektak XT profilometer. In the case of PCBM, the layer thickness of the films was determined via spectroscopic ellipsometry utilizing a Woolam WVASE ellipsometer. In order to determine the layer thickness, the ellipsometric data Psi and Delta were fitted only in the transparent regime of the material (1000 nm ≤ λ ≤ 1360 nm) utilizing the Cauchy dispersion formula.

Characterization—Contact Angle (θ_{contact}), Surface Free Energy (SFE) and Surface Tension (SFT): The wetting envelope, together with the polar and dispersive part of the SFE of a substrate are calculated with the measured θ_{contact} of three to four solvents (deionized water, diiodo

methane, ethylene glycol and/or dimethyl sulfoxide). θ_{contact} of sessile drops were measured (Krüss DSA 100 optical drop shape analyzer systems) with droplets ($\approx 2 \mu\text{L}$ or $0.5 \mu\text{L}$), which are obtained after a short time when the CA was static. The polar and dispersive parts of the SFE and SFT are calculated using Owens–Wendt–Rabel–Kaelble (OWRK) theory. For calculation of the polar and dispersive part of the SFT of the inks, the total SFT is measured with a pendant drop and the density and the sessile drop CA on a PTFE substrate.

Supporting Information

Supporting Information is available from the Wiley Online Library or from the author.

Acknowledgements

The financial support by the Federal Ministry for Research and Education (BMBF) through the project PRINTPERO (03SF0557A), the Initiating and Networking Funding of the Helmholtz Association (HYIG of U.W.P. (VH-NG-1148)); Recruitment Initiative of B.S.R.; the Helmholtz Energy Materials Foundry (HEMF); PEROSEED (ZT-0024); the project HYPer as part of HeiKa research collaboration; the Deutsche Forschungsgemeinschaft (DFG, German Research Foundation) under Germany's Excellence Strategy via the Excellence Cluster 3D Matter Made to Order (EXC-2082/1–390761711); and the Science and Technology of Nanostructures Research Program as well as the Karlsruhe School of Optics & Photonics (KSOP) is gratefully acknowledged. The authors would like to thank the members of the Perovskite Taskforce at LTI and IMT as well as the Printed Electronics research group at il for fruitful discussions and support in scientific work. The authors would like to express special gratitude toward Adrian Mertens, Ihtez M. Hossain and Yidenekachew J. Donie for supporting experimental work.

Author Contributions

The project was designed and conceptualized by F.S., H.E. and U.W.P. M.F. performed the XPS measurements and discussed the results. F.S. and H.E. performed the sample fabrication and all other characterization measurements, analyzed the data and wrote the first draft of the paper. B.S.R., U.W.P., G.H.-S., and U.L. supervised the overall conception. F.S. and H.E. contributed equally to this work. All authors contributed to the discussion of the results and in writing the manuscript.

Conflict of Interest

The authors declare no conflict of interest.

Keywords

charge transport layers, inkjet printing, perovskite solar cells, wetting behavior

Received: March 24, 2020

Revised: May 20, 2020

Published online:

[1] National Renewable Energy Laboratory (NREL), "Best Research-Cell Efficiencies," can be found under, <https://www.nrel.gov/pv/cell-efficiency.html> (accessed: March 2020).

- [2] K. Yoshikawa, H. Kawasaki, W. Yoshida, T. Irie, K. Konishi, K. Nakano, T. Uto, D. Adachi, M. Kanematsu, H. Uzu, K. Yamamoto, *Nat. Energy* **2017**, *2*, 17032.
- [3] F. Haase, C. Hollemann, S. Schäfer, A. Merkle, M. Rienäcker, J. Krügener, R. Brendel, R. Peibst, *Sol. Energy Mater. Sol. Cells* **2018**, *186*, 184.
- [4] W. Shockley, H. J. Queisser, *J. Appl. Phys.* **1961**, *32*, 510.
- [5] S. Rühle, *Sol. Energy* **2016**, *130*, 139.
- [6] T. Duong, H. Pham, T. C. Kho, P. Phang, K. C. Fong, D. Yan, Y. Yin, J. Peng, M. A. Mahmud, S. Gharibzadeh, B. A. Nejjand, I. M. Hossain, M. R. Khan, N. Mozaffari, Y. L. Wu, H. Shen, J. Zheng, H. Mai, W. Liang, C. Samundsett, M. Stocks, K. McIntosh, G. G. Andersson, U. Lemmer, B. S. Richards, U. W. Paetzold, A. Ho-Ballie, Y. Liu, D. Macdonald, A. Blakers, J. Wong-Leung, T. White, K. Weber, K. Catchpole, *Adv. Energy Mater.* **2020**, *10*, 1903553.
- [7] Helmholtz Zentrum Berlin, "World Record: Efficiency of perovskite silicon tandem solar cell jumps to 29.15 per cent," https://www.helmholtz-berlin.de/pubbin/news_seite?nid=21020;sprache=en;sei_tenid= (accessed: March 2020).
- [8] S. Gharibzadeh, I. M. Hossain, P. Fassl, B. A. Nejjand, T. Abzieher, M. Schultes, E. Ahlswede, P. Jackson, M. Powalla, S. Schäfer, M. Rienäcker, T. Wietler, R. Peibst, U. Lemmer, B. S. Richards, U. W. Paetzold, *Adv. Funct. Mater.* **2020**, *30*, 1909919.
- [9] T. Abzieher, J. A. Schwenzer, S. Moghadamzadeh, F. Sutterluti, I. M. Hossain, M. Pfau, E. Lotter, M. Hetterich, B. S. Richards, U. Lemmer, M. Powalla, U. W. Paetzold, *IEEE J. Photovoltaics* **2019**, *9*, 1249.
- [10] H. D. Pham, L. Gil-Escrig, K. Feron, S. Manzhos, S. Albrecht, H. J. Bolink, P. Sonar, *J. Mater. Chem. A* **2019**, *7*, 12507.
- [11] I. A. Howard, T. Abzieher, I. M. Hossain, H. Eggers, F. Schackmar, S. Ternes, B. S. Richards, U. Lemmer, U. W. Paetzold, *Adv. Mater.* **2019**, *31*, 1806702.
- [12] M. C. Tang, Y. Fan, D. Barrit, X. Chang, H. X. Dang, R. Li, K. Wang, D. M. Smilgies, S. F. Liu, S. De Wolf, T. D. Anthopoulos, K. Zhao, A. Amassian, *J. Mater. Chem. A* **2020**, *8*, 1095.
- [13] H. Hu, Z. Ren, P. W. K. Fong, M. Qin, D. Liu, D. Lei, X. Lu, G. Li, *Adv. Funct. Mater.* **2019**, *29*, 1900092.
- [14] J. Whitaker, D. Kim, B. W. Larson, F. Zhang, J. J. Berry, M. F. A. M. van Hest, K. Zhu, *Sustainable Energy Fuels* **2018**, *2*, 2442.
- [15] F. Di Giacomo, S. Shanmugam, H. Fledderus, B. J. Bruijners, W. J. H. Verhees, M. S. Dorenkamper, S. C. Veenstra, W. Qiu, R. Gehlhaar, T. Merckx, T. Aernouts, R. Andriessen, Y. Galagan, *Sol. Energy Mater. Sol. Cells* **2018**, *181*, 53.
- [16] Z. Wei, H. Chen, K. Yan, S. Yang, *Angew. Chem., Int. Ed.* **2014**, *53*, 13239.
- [17] C. Liang, P. Li, H. Gu, Y. Zhang, F. Li, Y. Song, G. Shao, N. Mathews, G. Xing, *Sol. RRL* **2018**, *2*, 1700217.
- [18] P. Li, C. Liang, B. Bao, Y. Li, X. Hu, Y. Wang, Y. Zhang, F. Li, G. Shao, Y. Song, *Nano Energy* **2018**, *46*, 203.
- [19] F. Mathies, T. Abzieher, A. Hochstuhl, K. Glaser, A. Colsmann, U. W. Paetzold, G. Hernandez-Sosa, U. Lemmer, A. Quintilla, *J. Mater. Chem. A* **2016**, *4*, 19207.
- [20] F. Mathies, E. J. W. List-Kratochvil, E. L. Unger, *Energy Technol.* **2019**, *8*, 1900991.
- [21] S. Schliske, M. Held, T. Rödlmeier, S. Menghi, K. Fuchs, M. Ruscello, A. J. Morfa, U. Lemmer, G. Hernandez-Sosa, *Langmuir* **2018**, *34*, 5964.
- [22] H. Eggers, F. Schackmar, T. Abzieher, Q. Sun, U. Lemmer, Y. Vaynzof, B. S. Richards, G. Hernandez-Sosa, U. W. Paetzold, *Adv. Energy Mater.* **2019**, *10*, 1903184.
- [23] B. Derby, *Annu. Rev. Mater. Res.* **2010**, *40*, 395.
- [24] T. M. Eggenhuisen, Y. Galagan, A. F. K. V. Biezemans, T. M. W. L. Slaats, W. P. Voorthuizen, S. Kommeren,

- S. Shanmugam, J. P. Teunissen, A. Hadipour, W. J. H. Verhees, S. C. Veenstra, M. J. J. Coenen, J. Gilot, R. Andriessen, W. A. Groen, *J. Mater. Chem. A* **2015**, 3, 7255.
- [25] X. Peng, J. Yuan, S. Shen, M. Gao, A. S. R. Chesman, H. Yin, J. Cheng, Q. Zhang, D. Angmo, *Adv. Funct. Mater.* **2017**, 27, 1703704.
- [26] N. Strobel, M. Seiberlich, R. Eckstein, U. Lemmer, G. Hernandez-Sosa, *Flexible Printed Electron.* **2019**, 4, 043001.
- [27] Chase Li, "Inkjet OLED Technology on the Verge of Mass Production, with Capacity Set to Rise 12-Fold from 2020 to 2024," <https://technology.ihc.com/615284/inkjet-oled-technology-on-the-verge-of-mass-production-with-capacity-set-to-rise-12-fold-from-2020-to-2024> (accessed: March 2020).
- [28] E. H., "Kateeva Introduces OLED RGB Pixel Deposition Line-up," <https://www.ledinside.com/products/2017/11/kateeva-introduces-oled-rgb-pixel-deposition-line-up> (accessed: March 2020).
- [29] R. Mertens, "BOE demonstrates a 55" 8K ink-jet printed OLED TV prototype," <https://www.oled-info.com/boe-demonstrates-55-8k-ink-jet-printed-oled-tv-prototype> (accessed: March 2020).
- [30] D. Zhao, W. Huang, L. Dong, Q. Jin, Y. Tian, G. Yuan, J. Ryu, L. Wang, *SID Int. Symp. Dig. Tech. Pap.* **2019**, 50, 945.
- [31] Z. Hu, Y. Yin, M. U. Ali, W. Peng, S. Zhang, D. Li, T. Zou, Y. Li, S. Jiao, S. J. Chen, C. Y. Lee, H. Meng, H. Zhou, *Nanoscale* **2020**, 12, 2103.
- [32] I. M. Hossain, D. Hudry, F. Mathies, T. Abzieher, S. Moghadamzadeh, D. Rueda-Delgado, F. Schackmar, M. Bruns, R. Andriessen, T. Aernouts, F. Di Giacomo, U. Lemmer, B. S. Richards, U. W. Paetzold, A. Hadipour, *ACS Appl. Energy Mater.* **2019**, 2, 47.
- [33] M. Singh, H. M. Haverinen, P. Dhagat, G. E. Jabbar, *Adv. Mater.* **2010**, 22, 673.
- [34] M. Rieu, M. Camara, G. Tournier, J. P. Viricelle, C. Pijolat, N. F. de Rooij, D. Briand, *Sens. Actuators, B* **2016**, 236, 1091.
- [35] N. Strobel, M. Seiberlich, T. Rödlmeier, U. Lemmer, G. Hernandez-Sosa, *ACS Appl. Mater. Interfaces* **2018**, 10, 42733.
- [36] A. Singh, S. K. Gupta, A. Garg, *Sci. Rep.* **2017**, 7, 1775.
- [37] M. Ruscello, T. Sarkar, A. Levitsky, G. M. Matrone, N. Droseros, S. Schliske, E. Sachs, P. Reiser, E. Mankel, W. Kowalsky, N. Banerji, N. Stingelin, G. L. Frey, G. Hernandez-Sosa, *Sustainable Energy Fuels* **2019**, 3, 1418.
- [38] A. Lange, M. Wegener, B. Fischer, S. Janietz, A. Wedel, in *Energy Procedia*, Elsevier Ltd, New York **2012**, pp. 150–158.
- [39] A. Gheno, J. Even, J. Bouclé, B. Ratier, S. Vedraïne, Y. Huang, A. Rolland, *Sol. RRL* **2018**, 2, 1800191.
- [40] X. Zheng, Y. Hou, C. Bao, J. Yin, F. Yuan, Z. Huang, K. Song, J. Liu, J. Troughton, N. Gasparini, C. Zhou, Y. Lin, D. J. Xue, B. Chen, A. K. Johnston, N. Wei, M. N. Hedhili, M. Wei, A. Y. Alsalloum, P. Maity, B. Turedi, C. Yang, D. Baran, T. D. Anthopoulos, Y. Han, Z. H. Lu, O. F. Mohammed, F. Gao, E. H. Sargent, O. M. Bakr, *Nat. Energy* **2020**, 5, 131.
- [41] R. Zhu, *Nat. Energy* **2020**, 5, 123.
- [42] D. Luo, R. Su, W. Zhang, Q. Gong, R. Zhu, *Nat. Rev. Mater.* **2020**, 5, 44.
- [43] E. Köhnen, M. Jošt, A. B. Morales-Vilches, P. Tockhorn, A. Al-Ashouri, B. Macco, L. Kegelmann, L. Korte, B. Rech, R. Schlattmann, B. Stannowski, S. Albrecht, *Sustainable Energy Fuels* **2019**, 3, 1995.
- [44] J. Xu, C. C. Boyd, Z. J. Yu, A. F. Palmstrom, D. J. Witter, B. W. Larson, R. M. France, J. Werner, S. P. Harvey, E. J. Wolf, W. Weigand, S. Manzoor, M. F. A. M. van Hest, J. J. Berry, J. M. Luther, Z. C. Holman, M. D. McGehee, *Science* **2020**, 367, 1097.
- [45] H. Chen, Q. Wei, M. I. Saidaminov, F. Wang, A. Johnston, Y. Hou, Z. Peng, K. Xu, W. Zhou, Z. Liu, L. Qiao, X. Wang, S. Xu, J. Li, R. Long, Y. Ke, E. H. Sargent, Z. Ning, *Adv. Mater.* **2019**, 31, 1903559.
- [46] C. Chen, S. Zhang, S. Wu, W. Zhang, H. Zhu, Z. Xiong, Y. Zhang, W. Chen, *RSC Adv.* **2017**, 7, 35819.
- [47] P. Docampo, J. M. Ball, M. Darwich, G. E. Eperon, H. J. Snaith, *Nat. Commun.* **2013**, 4, 2761.
- [48] J. C. Yu, J. A. Hong, E. D. Jung, D. Bin Kim, S. M. Baek, S. Lee, S. Cho, S. S. Park, K. J. Choi, M. H. Song, *Sci. Rep.* **2018**, 8, 1070.
- [49] Q. Zhao, R. Wu, Z. Zhang, J. Xiong, Z. He, B. Fan, Z. Dai, B. Yang, X. Xue, P. Cai, S. Zhan, X. Zhang, J. Zhang, *Org. Electron.* **2019**, 71, 106.
- [50] M. Saliba, J.-P. Correa-Baena, C. M. Wolff, M. Stollerfoht, N. Phung, S. Albrecht, D. Neher, A. Abate, *Chem. Mater.* **2018**, 30, 4193.
- [51] Y. Yao, W.-L. Hsu, M. Dagenais, *IEEE J. Photovoltaics* **2019**, 9, 1025.
- [52] L. Xu, X. Chen, J. Jin, W. Liu, B. Dong, X. Bai, H. Song, P. Reiss, *Nano Energy* **2019**, 63, 103860.
- [53] Z. Liu, J. Chang, Z. Lin, L. Zhou, Z. Yang, D. Chen, C. Zhang, S. (Frank) Liu, Y. Hao, *Adv. Energy Mater.* **2018**, 8, 1703432.
- [54] W. Chen, Y. Zhou, L. Wang, Y. Wu, B. Tu, B. Yu, F. Liu, H. W. Tam, G. Wang, A. B. Djurišić, L. Huang, Z. He, *Adv. Mater.* **2018**, 30, 1800515.
- [55] T. Abzieher, S. Moghadamzadeh, F. Schackmar, H. Eggers, F. Sutterlütli, A. Farooq, D. Kojda, K. Habicht, R. Schmager, A. Mertens, R. Azmi, L. Klohr, J. A. Schwenzer, M. Hetterich, U. Lemmer, B. S. Richards, M. Powalla, U. W. Paetzold, *Adv. Energy Mater.* **2019**, 9, 1802995.
- [56] H. Yoon, S. M. Kang, J. K. Lee, M. Choi, *Energy Environ. Sci.* **2016**, 9, 2262.
- [57] T. Abzieher, S. Moghadamzadeh, F. Schackmar, H. Eggers, F. Sutterlütli, A. Farooq, D. Kojda, K. Habicht, R. Schmager, A. Mertens, R. Azmi, L. Klohr, J. A. Schwenzer, M. Hetterich, U. Lemmer, B. S. Richards, M. Powalla, U. W. Paetzold, *Adv. Energy Mater.* **2019**, 9, 1802995.
- [58] S. F. Völker, S. Collavini, J. L. Delgado, *ChemSusChem* **2015**, 8, 3012.
- [59] K. Wojciechowski, T. Leijtens, S. Siprova, C. Schlueter, M. T. Hörantner, J. T. W. Wang, C. Z. Li, A. K. Y. Jen, T. L. Lee, H. J. Snaith, *J. Phys. Chem. Lett.* **2015**, 6, 2399.
- [60] D. Rueda-Delgado, I. M. Hossain, M. Jakoby, J. A. Schwenzer, T. Abzieher, I. A. Howard, B. S. Richards, U. Lemmer, U. W. Paetzold, *Org. Electron.* **2019**, 105526.
- [61] S. Collavini, I. Kosta, S. F. Völker, G. Cabanero, H. J. Grande, R. Tena-Zaera, J. L. Delgado, *ChemSusChem* **2016**, 9, 1263.
- [62] C. Liu, Y. Yang, Y. Ding, J. Xu, X. Liu, B. Zhang, J. Yao, T. Hayat, A. Alsaedi, S. Dai, *ChemSusChem* **2018**, 11, 1232.
- [63] W. Kang, M. Kitamura, Y. Arakawa, *Org. Electron.* **2013**, 14, 644.
- [64] N. Reis, B. Derby, *MRS Proc.* **2000**, 625, 117.
- [65] T. Jeon, S. J. Kim, J. Yoon, J. Byun, H. R. Hong, T. W. Lee, J. S. Kim, B. Shin, S. O. Kim, *Adv. Energy Mater.* **2017**, 7, 1602596.
- [66] G. Cai, P. Darmawan, M. Cui, J. Chen, X. Wang, A. L. S. Eh, S. Magdassi, P. S. Lee, *Nanoscale* **2016**, 8, 348.
- [67] C.-C. Huang, Z.-K. Kao, Y.-C. Liao, *ACS Appl. Mater. Interfaces* **2013**, 5, 12954.
- [68] C. C. Huang, P. C. Su, Y. C. Liao, in *Thin Solid Films*, Elsevier B.V., New York **2013**, pp. 348–351.
- [69] H. Hu, J. Zhu, M. Chen, T. Guo, F. Li, *Appl. Surf. Sci.* **2018**, 441, 295.
- [70] R. Brisse, R. Faddoul, T. Bourgeteau, D. Tondelier, J. Leroy, S. Campidelli, T. Berthelot, B. Geoffroy, B. Jusselme, *ACS Appl. Mater. Interfaces* **2017**, 9, 2369.
- [71] J. R. Manders, S.-W. Tsang, M. J. Hartel, T.-H. Lai, S. Chen, C. M. Amb, J. R. Reynolds, F. So, *Adv. Funct. Mater.* **2013**, 23, 2993.
- [72] S. Hietzschold, S. Hillebrandt, F. Ullrich, J. Bombsch, V. Rohnacher, S. Ma, W. Liu, A. Köhn, W. Jaegermann, A. Pucci, W. Kowalsky, E. Mankel, S. Beck, R. Lovrincic, *ACS Appl. Mater. Interfaces* **2017**, 9, 39821.
- [73] N. Nishimoto, Y. Yamada, Y. Ohnishi, N. Imawaka, K. Yoshino, *Phys. Status Solidi A* **2013**, 210, 589.
- [74] Y. N. Kim, H. G. Shin, J. K. Song, D. H. Cho, H. S. Lee, Y. G. Jung, *J. Mater. Res.* **2005**, 20, 1574.

- [75] R. G. Gordon, *MRS Bull.* **2000**, 25, 52.
- [76] X. Yin, M. Que, Y. Xing, W. Que, *J. Mater. Chem. A* **2015**, 3, 24495.
- [77] H. C. Nallan, J. A. Sadie, R. Kitsomboonloha, S. K. Volkman, V. Subramanian, *Langmuir* **2014**, 30, 13470.
- [78] D. K. Owens, R. C. Wendt, *J. Appl. Polym. Sci.* **1969**, 13, 1741.
- [79] W. Rabel, *Farbe Lack* **1971**, 77, 997.
- [80] D. H. Kaelble, *J. Adhes.* **1970**, 2, 66.
- [81] A. P. Grosvenor, M. C. Biesinger, R. S. C. Smart, N. S. McIntyre, *Surf. Sci.* **2006**, 600, 1771.
- [82] B. P. Payne, M. C. Biesinger, N. S. McIntyre, *J. Electron Spectrosc. Relat. Phenom.* **2009**, 175, 55.
- [83] S. Tengeler, M. Fingerle, W. Calvet, C. Steinert, B. Kaiser, T. Mayer, W. Jaegermann, *J. Electrochem. Soc.* **2018**, 165, H3122.
- [84] M. Fingerle, S. Tengeler, W. Calvet, T. Mayer, W. Jaegermann, *J. Electrochem. Soc.* **2018**, 165, H3148.
- [85] J. C. De Jesus, I. González, A. Quevedo, T. Puerta, *in J. Mol. Catal. A: Chem.* **2005**, 228, 283.
- [86] K. Wang, Y. Tian, H. Jiang, M. Chen, S. Xu, *Int. J. Photoenergy* **2019**, 2019, 1.
- [87] D. Di Girolamo, F. Matteocci, F. U. Kosasih, G. Chistiakova, W. Zuo, G. Divitini, L. Korte, C. Ducati, A. Di Carlo, D. Dini, A. Abate, *Adv. Energy Mater.* **2019**, 9, 1901642.
- [88] P. W. Liang, C. Y. Liao, C. C. Chueh, F. Zuo, S. T. Williams, X. K. Xin, J. Lin, A. K. Y. Jen, *Adv. Mater.* **2014**, 26, 3748.
- [89] Q. Chen, H. Zhou, T. Bin Song, S. Luo, Z. Hong, H. S. Duan, L. Dou, Y. Liu, Y. Yang, *Nano Lett.* **2014**, 14, 4158.
- [90] L. Wang, C. McCleese, A. Kovalsky, Y. Zhao, C. Burda, *J. Am. Chem. Soc.* **2014**, 136, 12205.
- [91] S. Liu, W. Huang, P. Liao, N. Pootrakulchote, H. Li, J. Lu, J. Li, F. Huang, X. Shai, X. Zhao, Y. Shen, Y. B. Cheng, M. Wang, *J. Mater. Chem. A* **2017**, 5, 22952.
- [92] D. Yang, X. Zhang, K. Wang, C. Wu, R. Yang, Y. Hou, Y. Jiang, S. Liu, S. Priya, *Nano Lett.* **2019**, 19, 3313.
- [93] O. Malinkiewicz, A. Yella, Y. H. Lee, G. M. Espallargas, M. Graetzel, M. K. Nazeeruddin, H. J. Bolink, *Nat. Photonics* **2014**, 8, 128.
- [94] Y. Zheng, J. Kong, D. Huang, W. Shi, L. Mcmillon-Brown, H. E. Katz, J. Yu, A. D. Taylor, *Nanoscale* **2018**, 10, 11342.
- [95] C. H. Chiang, C. G. Wu, *Nat. Photonics* **2016**, 10, 196.
- [96] C. Zuo, L. Ding, *Adv. Energy Mater.* **2017**, 7, 1601193.
- [97] C. N. Hoth, S. A. Choulis, P. Schilinsky, C. J. Brabec, *Adv. Mater.* **2007**, 19, 3973.
- [98] C. N. Hoth, P. Schilinsky, S. A. Choulis, C. J. Brabec, *Nano Lett.* **2008**, 8, 2806.
- [99] C. N. Hoth, S. A. Choulis, P. Schilinsky, C. J. Brabec, *J. Mater. Chem.* **2009**, 19, 5398.
- [100] T. Aernouts, T. Aleksandrov, C. Girotto, J. Genoe, J. Poortmans, *Appl. Phys. Lett.* **2008**, 92, 033306.
- [101] J. Seo, S. Park, Y. Chan Kim, N. J. Jeon, J. H. Noh, S. C. Yoon, S. Il Seok, *Energy Environ. Sci.* **2014**, 7, 2642.
- [102] D. X. Yuan, X. D. Yuan, Q. Y. Xu, M. F. Xu, X. B. Shi, Z. K. Wang, L. S. Liao, *Phys. Chem. Chem. Phys.* **2015**, 17, 26653.
- [103] D. Boucher, J. Howell, *J. Phys. Chem. B* **2016**, 120, 11556.
- [104] P. Li, C. Liang, B. Bao, Y. Li, X. Hu, Y. Wang, Y. Zhang, F. Li, G. Shao, Y. Song, *Nano Energy* **2018**, 46, 203.
- [105] F. Mathies, H. Eggers, B. S. Richards, G. Hernandez-Sosa, U. Lemmer, U. W. Paetzold, *ACS Appl. Energy Mater.* **2018**, 1, 1834.
- [106] D. C. Miller, J. Bengoechea, J. G. Bokria, M. Köhl, N. E. Powell, M. E. Smith, M. D. White, H. R. Wilson, J. H. Wohlgemuth, *in Reliability of Photovoltaic Cells, Modules Components, Systems VI*, International Society For Optics And Photonics, Bellingham, WA **2013**, p. 882509.
- [107] A. Klein, T. Mayer, A. Thissen, W. Jaegermann, *Bunsenmagazin* **2008**, 10, 124.
- [108] D. A. Shirley, *Phys. Rev. B* **1972**, 5, 4709.
- [109] A. Proctor, P. M. A. Sherwood, *Anal. Chem.* **1982**, 54, 13.